The 9th European Congress on Computational Methods in Applied Sciences and Engineering
ECCOMAS Congress 2024
3–7 June 2024, Lisboa, Portugal

BUOYANT HIGH-PRESSURE TRANSCRITICAL FLUID DUCT FLOWS

C. MONTEIRO[1] AND L. JOFRE[1]

[1] Department of Fluid Mechanics
Universitat Politècnica de Catalunya · BarcelonaTech (UPC), Barcelona 08019, Spain
e-mails: carlos.alexandre.bandarrinha.m@upc.edu, lluis.jofre@upc.edu

Key words: Buoyancy effects, Supercritical fluids, Turbulent square duct

Summary. In this work, direct numerical simulations of a high-pressure transcritical square duct flow with distinct gravity directions in the cross-stream plane are performed. The buoyancy effects on the instantaneous and mean fields are analyzed. Significant differences are highlighted in the distributions of Prandtl's second-kind motions due to a strong coupling effect between the high-pressure transcritical phenomena and the buoyancy effects. The observed phenomena indicate that prior characterizations of secondary flows and their contribution to heat and mass transfer (commonly considered as independent from the Reynolds number) do not apply in cases above the critical regime where strong variations in thermophysical properties are found. Furthermore, the number and dynamics of these secondary flows are significantly affected by the gravity direction.

1 INTRODUCTION

Wall-bounded fluid flows surpassing the critical pressure are gaining prominence in advanced energy systems like power generation and propulsion [6, 22, 23, 2], where heat convection is the prominent mechanism. When subjected to a temperature difference that oscillates around the pressure-specific critical temperature, these supercritical fluids exhibit a diffuse transition region. This region separates the liquid-like and gas-like supercritical phases without the physical boundary observed under standard (subcritical pressure) thermodynamic conditions. Moreover, this transition region is characterized by: (i) sharp gradients in thermophysical properties, such as density (ρ), viscosity (μ), and diffusivity (α); (ii) intensified fluctuations of fluid properties; and (iii) induced flow rotation through the baroclinic torque generated [4, 3, 11, 1].

Ducts with rectangular cross-sections are prevalent in numerous engineering applications, encompassing both incompressible and compressible turbulent flow regimes. These flows are characterized by the presence of secondary motions in the cross-stream plane, which significantly influence the overall flow dynamics and system performance. In straight square ducts, secondary motions of Prandtl's second kind emerge due to anisotropic turbulent stresses [19], forming eight counter-rotating vortices near the corners. Although these motions in traditional flows exhibit an intensity significantly lower than the bulk velocity ($\sim 1-2\%$), they persist throughout the flow, contributing to mean duct friction by up to a few percent and significantly enhancing the transverse transfer of mass, momentum, and heat [12]. Additionally, temperature asymmetries and gradients near asymmetrically heated corners in high-pressure transcritical square duct flows, as studied by Monteiro & Jofre [13], introduce complexities that significantly

influence secondary flow motions. These temperature variations modulate wall shear stresses via secondary flow motions, thereby impacting the overall flow behavior.

While Sekimoto et al. [20] investigated the effect of cross-sectional buoyancy in asymmetrically heated, incompressible square ducts, the interaction between these effects and the strong variations of fluid properties in high-pressure transcritical square ducts remains unexplored. In this context, the present work aims to analyze the consequences of varying gravity directions on the flow characteristics of high-pressure transcritical turbulent square duct flows. Particular focus is given to the effects of secondary flow motions, which serve as indicators of the turbulence state in straight square ducts. To that end, in Section 2, the flow physics modeling of supercritical fluids and the description of the numerical experiments are presented. Next, the numerical results are presented in Section 3. Finally, in Section 4, the work is concluded, and future directions are proposed.

2 COMPUTATIONAL APPROACH & SIMULATIONS

This section outlines the framework utilized for studying supercritical fluids, focusing on (i) the equations of fluid motion, (ii) real-gas thermophysical models, and (iii) the case setups and descriptions. The numerical method and real-gas thermodynamics framework employed in this study follow the approach detailed by Monteiro et al. [13]. Specifically, the Peng-Robinson equation of state is utilized, and a second-order central-differencing scheme is implemented, along with a third-order Runge-Kutta time integration method.

2.1 Equations of Fluid Motion

The flow motion of supercritical fluids is described by the following set of dimensionless conservation equations of mass, momentum, and total energy

$$\frac{\partial \rho^\star}{\partial t^\star} + \nabla^\star \cdot (\rho^\star \mathbf{v}^\star) = 0, \tag{1}$$

$$\frac{\partial (\rho^\star \mathbf{v}^\star)}{\partial t^\star} + \nabla^\star \cdot (\rho^\star \mathbf{v}^\star \mathbf{v}^\star) = -\nabla^\star P^\star + \frac{\nabla^\star \cdot \boldsymbol{\tau}^\star}{Re_b} + \left(Ri_b + \frac{1}{Fr_b^2} \right) \hat{\mathbf{e}}_g, \tag{2}$$

$$\frac{\partial (\rho^\star E^\star)}{\partial t^\star} + \nabla^\star \cdot (\rho^\star \mathbf{v}^\star E^\star) = \frac{\nabla^\star \cdot (\kappa^\star \nabla^\star T^\star)}{Re_b Br_b} - \nabla^\star \cdot (P^\star \mathbf{v}^\star) + \frac{\nabla^\star \cdot (\boldsymbol{\tau}^\star \cdot \mathbf{v}^\star)}{Re_b} + \left(Ri_b + \frac{1}{Fr_b^2} \right) \mathbf{v}^\star \hat{\mathbf{e}}_g, \tag{3}$$

where superscript $\star$ denotes normalized quantities, $\rho = \rho_b + \Delta\rho$ represents the density, t is the time, $\mathbf{v}$ is the velocity vector, and P is the pressure. The viscous stress tensor is defined as $\boldsymbol{\tau} = \mu \left(\nabla \mathbf{v} + \nabla \mathbf{v}^T \right) - (2\mu/3)(\nabla \cdot \mathbf{v}) \boldsymbol{I}$, with μ being the dynamic viscosity and $\boldsymbol{I}$ the identity matrix. The gravity unit vector is denoted by $\hat{\mathbf{e}}_g$, while $E = e + |\mathbf{v}|^2/2$ and e represent the total and internal energy, respectively. Additionally, T is the temperature, and κ is the thermal conductivity. The obtention of these dimensionless equations is founded on the following set of inertial-based scalings [8, 7]

$$\mathbf{x}^\star = \frac{\mathbf{x}}{D_h}, \quad \mathbf{v}^\star = \frac{\mathbf{v}}{u_b}, \quad \rho^\star = \frac{\rho}{\rho_b}, \quad T^\star = \frac{T}{T_b}, \tag{4}$$

$$P^\star = \frac{P}{\rho_b u_b^2}, \quad E^\star = \frac{E}{u_b^2}, \quad \mu^\star = \frac{\mu}{\mu_b}, \quad \kappa^\star = \frac{\kappa}{\kappa_b},$$

with subscript b indicating bulk quantities, $\mathbf{x}$ the position vector, D_h the hydraulic diameter, and u_b the bulk streamwise velocity. The resulting set of scaled equations includes four dimensionless numbers: (i) the bulk Reynolds number $Re_b = \rho_b u_b D_h/\mu_b$ characterizes the ratio between inertial and viscous forces; (ii) the bulk Brinkman number $Br_b = Pr_b Ec_b$ relates heat produced by viscous dissipation and heat transported by molecular conduction. Specifically, the bulk Prandtl number $Pr_b = \mu_b c_{Pb}/\kappa_b$, where c_P is the isobaric heat capacity, quantifies the ratio between momentum and thermal diffusivity. The bulk Eckert number $Ec_b = u_b^2/(c_{Pb}T_b)$ accounts for the ratio between advective mass transfer and heat dissipation potential; (iii) the Richardson number $Ri_b = Gr_b/Re_b^2$ represents the importance of natural convection relative to forced convection, where the Grashof number $Gr_b = \Delta\rho/\rho_b \cdot D_h/\nu_b^2 \cdot g$ quantifies the relative significance of buoyancy forces compared to viscous forces in the fluid flow when subjected to a temperature gradient; and (iv) the Froude number $Fr_b = u/\sqrt{gD_h}$ which defines the ratio between flow inertia and the gravity field.

2.2 Flow conditions and simulation setup

In this work, four square-duct flow cases with distinct gravity directions are analyzed under similar high-pressure transcritical thermophysical conditions. The operating fluid corresponds to CO_2, whose critical pressure and temperature are $P_c = 7.4\,\mathrm{MPa}$ and $T_c = 304.1\,\mathrm{K}$, respectively. Each case maintains a pseudo-boiling region within the duct flow. To achieve this, the bulk pressure is set to $P_b/P_c = 2$, the top-hot wall-temperature is fixed at $T_{\mathrm{hw}}/T_c = 1.5$, and the remaining physical walls are set to $T_{\mathrm{cw}}/T_c = 0.85$. The streamwise boundaries for all cases are periodic, the bulk velocity is $u_b = 0.5$ m/s, and the hydraulic diameter is $D_h = 2\delta$ where $\delta = 500$ μm. These conditions result in a Richardson number of $Ri_b \approx 0.04$ and a Froude number of $Fr \approx 5.2$, comparable to the ones in the intermediate case of Sekimoto et al. [20]. This indicates that the effects of external forcing due to gravity account for approximately 5% of the flow modulation relative to flow inertia. Given that these effects act in the cross-sectional direction, their influence is expected to be particularly significant for the secondary flow motions. Therefore, to scrutinize the effects of gravity in these systems, the primary distinction between the four cases is the direction of gravity.

Table 1 presents the case identification, the corresponding gravity direction (or absence of gravity), and additional characterization details, such as the bulk Reynolds number (Re_b), the friction Reynolds numbers based on cold-bottom ($Re_{\tau_{\mathrm{cw}}}$) and hot-top wall units ($Re_{\tau_{\mathrm{hw}}}$), the bulk Prandtl number (Pr_b), the hot-top wall Nusselt number (Nu_{hw}), and the maximum relative intensity of the mean cross-stream flow ($\sqrt{(\bar{v}^2 + \bar{w}^2)}/u_{b_{max}}$). The first case is configured without a gravity component, serving as a reference point, thus enabling the analysis of the impact of different gravity directions on the turbulence state. Specifically, case 2-mYG features gravity in the negative y-direction, case 3-YG features gravity in the positive y-direction, and case 4-ZG features gravity in the z-direction. In addition, a mesh resolution investigation, similar to the one conducted by Monteiro & Jofre [13], is performed to ensure that all relevant flow scales are resolved. The spatial discretization is meticulously designed to ensure that: (i) the first grid point is placed at a maximum distance of $y^* < 1.0$ from the hot wall and $y^* < 0.6$ from the cold wall; (ii) resolutions normalized by the Kolmogorov scale are $\Delta x/\eta_u < 9$, $\Delta y/\eta_u < 2$ and

$\Delta z/\eta_u < 2$; and (iii) the resolutions normalized by the Batchelor scale are $\Delta x/\eta_T < 10$, $\Delta x/\eta_T < 2$ and $\Delta x/\eta_T < 2$. Notably, all these values fall within the accepted ranges in the literature for the direct numerical simulation (DNS) of high-pressure transcritical wall-bounded flows [17, 10, 6].

Table 1: Classification of the four numerical experiments along with their thermodynamic operating conditions and resulting dimensionless parameters. The table includes the approximate bulk Reynolds number Re_b, the perimeter-averaged friction Reynolds number for the hot-top and cold-bottoms walls Re_τ, the bulk Prandtl number Pr_b, the hot wall Nusselt number Nu_{hw}, and the maximum value of the mean cross-sectional velocity intensity normalized by the bulk velocity $\sqrt{(\bar{v}^2 + \bar{w}^2)}/u_{b_{max}}$.

Case	Symbol	$\hat{\mathbf{e}}_g$	Re_b	$Re_{\tau_{\text{cw}}}$	$Re_{\tau_{\text{hw}}}$	Pr_b	Nu_{hw}	$\sqrt{(\bar{v}^2 + \bar{w}^2)}/u_{b_{max}}$
1 - NoG	○	(0, 0, 0)	4400	110	200	1.83	47.3	0.046
2 - mYG	△	(0, $-g$, 0)	4200	100	200	1.81	42.0	0.040
3 - YG	□	(0, g, 0)	4600	120	210	1.84	52.9	0.062
4 - ZG	◇	(0, 0, g)	4300	110	210	1.80	76.5	0.095

3 RESULTS

From Table 1, the general characteristics of each flow case can be discerned. A particular focus is placed on the hot-top wall, as it is the most relevant in terms of heat transfer. Initially, the bulk Reynolds number Re_b reveals that gravity's effect in the y-direction significantly influences inertial effects depending on its orientation: gravity pointing towards the hot wall (up) exacerbates inertial effects, while gravity pointing away (down) mitigates them. This observed trend is mirrored in other parameters such as the friction Reynolds number $Re_{\tau_{\text{hw}}}$, the bulk Prandtl number (Pr_b), the hot-wall Nusselt number (Nu_{hw}), and the maximum cross-stream velocity intensity $\sqrt{(\bar{v}^2 + \bar{w}^2)}/u_{b_{max}}$. Interestingly, when gravity is aligned parallel to the hot wall (Case 4-ZG), the behavior of these quantities is distinct. Specifically, while Re_b and Pr_b exhibit slight reductions, a notable increase in $Re_{\tau_{\text{hw}}}$ is observed. This suggests that Case 4-ZG, despite having a generally less turbulent core flow, experiences localized turbulence enhancements near the hot wall. Notably, both the hot-wall Nusselt number and the maximum cross-stream velocity intensity are significantly elevated in this case, even surpassing those observed in Case 3-YG, where positive y gravity direction ostensibly enhances mixing and heat transfer. The subsequent analysis will delve into the effects of varying gravity directions on: (i) the mean Prandtl number distribution, (ii) distributions of hot-top wall quantities, and (iii) secondary flow motions.

3.1 Mean Fluid Properties

Figure 1 illustrates the mean variation in the Prandtl number across different cases. Due to the symmetry along the $z/\delta = 1$ plane for the first three cases, only half x-averaged sections of the mean quantities are presented. In contrast, for Case 4-ZG, the full averaged section is necessary to capture the complete distribution. In general, the cases exhibit a notably thin gas-like region at the hot-top wall, characterized by Prandtl numbers less than unity. In this region,

the fluid displays lower ρ, μ, κ, but higher thermal diffusivity α [13]. This region of maximum Prandtl defines the boundaries of the pseudo-boiling zone, which shows different topological features depending on the gravity direction. As anticipated, at lower Re_b, where buoyancy effects are significant, the distribution of fluid and flow properties becomes noticeably affected. This observation suggests that, under the conditions investigated, the interplay between buoyancy-driven and corner-dependent secondary flow motions influences the distribution of bulk fluid properties and, consequently, the flow characteristics. This is in contrast to the minimal effects of secondary flow motions of bulk properties, as typically observed in incompressible flows [19].

Additional insights can be extracted from Figure 1 by comparing each case individually to the reference case (1-NoG). In Case 2-mYG, where gravity acts in the negative y gravity direction, the colder denser fluid accumulates in the bottom region. This configuration supports flow stability and enhances the separation between the two supercritical regimes. The presence of denser fluid at the bottom promotes steadiness and helps maintain the delineation between the gas-like and liquid-like phases. In contrast, Case 3-YG, with gravity directed positively along y, sees the denser fluid migrating towards the hotter regions, where lighter fluid is encountered. This movement intensifies mixed convection, thereby increasing the depth of the region characterized by higher momentum and thermal diffusivity within the core flow. Consequently, this configuration enhances both mixing and heat transfer. Finally, Case 4-ZG demonstrates a distinct asymmetric behavior in which the highest Prandtl numbers are observed near the top left corner. This pattern aligns with the migration of lighter gas-like supercritical fluid towards the top wall and lateral wall, while the denser liquid-like fluid shifts to the opposite lateral wall. This configuration fosters a more pronounced counter-clockwise recirculation of the fluid.

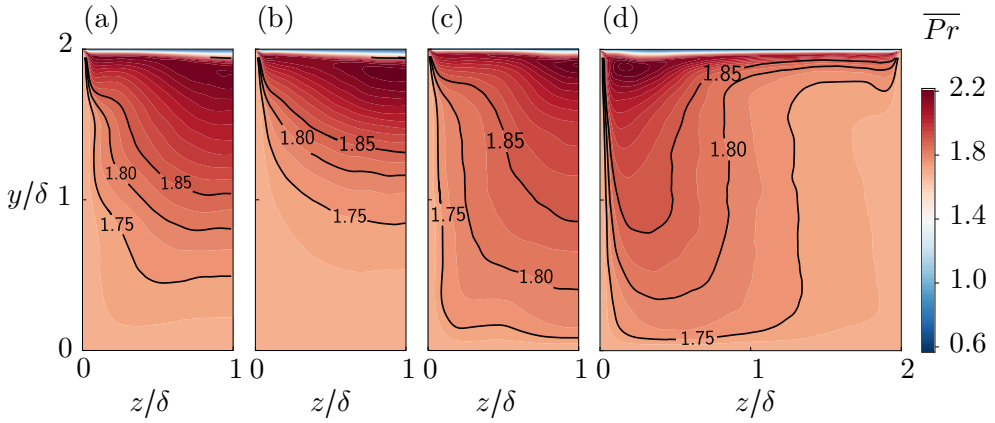

Figure 1: Spatial distribution with isolines of mean Prandtl number for cases D192Nog (a), D192mY (b), D192Y (d), and D192Z (d).

3.2 Hot-Wall Distributions

Figure 4 illustrates the hot wall distribution of wall shear stresses normalized by the mean value τ_w/τ_p and the local wall Nusselt number $Nu_{\text{loc}} = D_h\kappa_{\text{loc}}/\kappa_w \frac{\partial \bar{T}_w}{\partial n} / \left(\bar{T}_w - T_b\right)$, as defined by Nemati et al. [14]. In examining the distribution of wall shear stresses for cases 1 through 3, a pattern typical of turbulent square duct flows emerges. Specifically, a double peak is observed

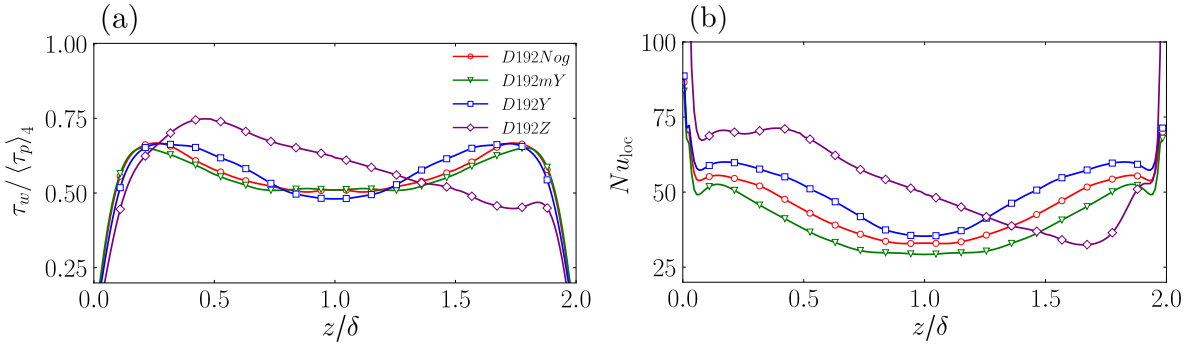

Figure 2: Hot wall distributions of wall shear stress normalized by the perimeter-averaged wall-shear stress (a) and the local Nusselt number (b).

near the perpendicular walls, with a local minimum at the center coordinate (z/δ = 1). As $Re_{\tau_{\mathrm{hw}}}$ increases, these peaks slightly shift towards the center, and the local minimum becomes slightly lower. This behavior contrasts with fully developed turbulent cases of ideal-gas and incompressible duct flows at comparable Reynolds numbers [19, 18]. For instance, in the studies by Pinelli et al.[18, 15], the local minimum at $z/\delta = 1$ is evident only at lower Reynolds numbers ($Re_b \sim 1000 - 2000$), corresponding to the marginally turbulent regimes described by Uhlmann et al.[21]. This suggests that, despite achieving Re_b and $Re_{\tau_{\mathrm{hw}}}$ indicative of fully developed flow due to the nuanced distribution of supercritical thermophysical properties, the near-wall region of cases 1 to 3 exhibits characteristics of marginally turbulent (lower Re_b) scenarios. As noted in the literature [13], the turbulent-like state of high-pressure transcritical ducts is predominantly triggered by the presence of a pseudo-transition, whereas at low pressure but under the same flow conditions, the flow would present characteristics of a fully laminar flow. This indicates that flow disturbances in high-pressure transcritical ducts are primarily driven by magnified gradients of thermophysical properties and flow rotation induced by baroclinic torque [3]. Consequently, these observations reveal that the behavior of near-wall flow in high-pressure transcritical duct flows diverges significantly from incompressible scenarios, even at comparable Reynolds numbers. Supporting this assumption, the wall shear stress distribution in case 4-ZG exhibits a markedly different shape, underscoring the substantial impact of buoyancy-driven and corner-dependent secondary flow motions on the mean streamwise flow. In this scenario, the maximum discrepancy compared to the normalized peak in case 1-NoG is approximately 20%. Furthermore, the Nusselt number distributions corroborate these conclusions.

As a consequence of the specific shape of the wall-shear stress distributions, the streamwise velocity field is locally affected. Therefore, Figure 3 displays the distribution of streamwise velocity profiles from the hot wall to the cold wall in semi-local wall units [16] from the top wall. These distributions vary along the z/δ coordinates, with each line representing a different z/δ position. Specifically, the red line corresponds to the first grid line parallel to the lateral wall, the purple line corresponds to the center of the duct ($z/\delta = 1$), while the grey, blue, and green lines represent intermediate positions. Figure 3 also includes an inset showing the corresponding streamwise velocity field and the locations where the profile data were acquired. Significant differences in the overall field and the velocity profiles are noticeable. The location of peak velocity and the extent of the higher velocity region (focusing on the extent of the isocontours)

shift according to the Prandtl number distributions. Notably, the peak velocity is approximately located at the pseudo-boiling region.

Regarding the hot-wall velocity profiles, especially by examining the midplane $z/\delta = 1$ distributions highlighted in purple, the region of logarithmic behavior can be identified, indicating a higher level of turbulent/inertial effects. As expected, the magnitude and shape of the profiles become increasingly attenuated as the z/δ coordinate approaches the vertical wall ($z/\delta \approx 0$). However, it is important to note that beyond the viscous sub-layer ($y^*_{\mathrm{hw}} > 5$), these profiles fall significantly below the laws of the wall that approximate the established square duct results from Gavrilakis [5]. Additionally, the intermediate profiles (blue, green, and red lines) present significantly different shapes, exhibiting local peaks and valleys. This can be generally attributed to: (i) the lower hot-wall shear stress, especially when compared to the cold walls of the duct ($\tau_{\mathrm{hw}}/\tau_p < 1$); and (ii) the substantial influence of secondary flow motions on the streamwise velocity component. It is known from the analysis of incompressible scenarios at high enough Reynolds numbers that the self-regulating mechanism of secondary flow motions is responsible for promoting the collapse of the velocity profiles onto the known wall-laws [19]. In incompressible cases at very low Reynolds numbers, a slight overshoot of u^+ is usually seen due to the local minimum in wall-shear stress [18, 15]. Contrarily, in this study, the overshoot characteristic of marginally turbulent square duct scenarios is predominantly observed in the distribution of cold wall velocity profiles, coinciding with higher values of wall shear stress (omitted for brevity). Therefore, the resulting shape of the velocity profiles in Fig. 3 is likely due to the coupling of real-fluid effects [9] and buoyancy-driven secondary flow motions. Interestingly, the three most interior highlighted profiles of case 4-ZG (purple, blue, and green) exhibit a better collapse compared to the other cases. This suggests that the intensified/larger buoyancy-driven secondary flow assists in the mentioned self-regulating mechanism of secondary flow motions on the streamwise velocity component. It is worth mentioning that the shape of these profiles still displays a less logarithmic-like behavior compared to the cases with higher Re_b values, namely cases 1-NoG and 3-YG. This indicates that a trade-off effect between wall-shear stress redistribution and turbulence production exists in case 4-ZG towards the region of more intensified pseudo-boiling activity ($z/\delta \approx 0$).

3.3 Secondary Flow Motions

Figure 4 presents the resulting mean cross-flow intensity with vectors of the cross-stream velocity components v and w and the streamwise vorticity. Due to spatial changes in mean thermophysical properties, the fluid is propelled in different cross-stream directions. Consequently, the traditional concept of the eight symmetric contour rotating streamwise vortices, typically visible in fully developed square ducts, is altered. These secondary flow motions, which would otherwise result from the anisotropic distribution of Reynolds stresses in a turbulent incompressible square duct flow, now also arise from cross-stream buoyancy-driven flows. Generally, the cases show agreement with literature [13] regarding the positioning of higher cross-stream velocity intensity in the hot wall region. Furthermore, the shape of the main counter-rotating vortex pairs in the top and bottom walls remains similar among cases 1-NoG, 2-mYG, and 3-YG. However, as assessed from Table 1, the maximum intensity of the secondary flows in cases 3-YG and 4-ZG increases significantly. Specifically, it increases by roughly 35% and 100% from case 1-NoG to case 3-YG and 4-ZG, respectively. From Figure 4 (e) to (h), it is observed that the

center of the maximum vorticity secondary motion, indicated by the yellow circle, moves away from the corner non-monotonically with the increase of maximum intensity as Re_b increases. This suggests that the topology of the secondary motions is dependent on the gravity directions and the resulting real-fluid effects rather than the Reynolds number. Conversely, under the conditions explored, the maximum intensity of the secondary flow motions is monotonically dependent on the Reynolds number. This finding contrasts with previous investigations of low-pressure isothermal literature [19], where the intensity of the secondary flow motions is approximately $1-2\%$ of the bulk flow (independent of the Reynolds number), and their center penetrates slightly further towards the corner with increasing Re_b.

Investigating Figure 4 in more detail, it can be observed additional important behaviors associated with different gravity directions. (i) Case 1-NoG presents a more uniform distribution of peripheral secondary flow motions, with intermediate intensity and a higher number of streamwise vortices compared to the other cases. The bottom corner vortex pair is approximately symmetric with respect to the duct bisector, indicating that the liquid-like supercritical region aligns more closely with incompressible flow scenarios. (ii) Case 2-mYG shows more intense secondary flow motions uniquely in the top region. This intensity is possibly explained by the strong confinement of the pseudo-boiling region due to gravity, as observed in the Prandtl number distribution in Fig. 1. (iii) Case 3-YG displays a closer similarity in the secondary flow motions in the hot and cold halves of the duct (separated by $y/\delta = 1$). Despite this symmetry in topology, significantly higher intensity and vorticity are found near the pseudo-boiling region. (iv) Case 4-ZG showcases a major secondary vortex of size D_h, similar to the findings of Sekimoto et al. [20]. In addition, smaller counter-rotating vortices are accommodated near the corners. The highest intensity region is mainly situated near the hot-top wall region. This enhances chaotic mixing near the walls, associated with the increased transversal flow near the wall, which elevates enstrophy.

4 CONCLUSIONS

This investigation employed DNS to examine the impact of gravity direction on low Reynolds number turbulent flows in high-pressure transcritical square ducts. The findings illustrate that gravity direction profoundly influences various flow characteristics, including the bulk Reynolds number, friction Reynolds number, and hot-wall Nusselt number. Notably, when gravity is aligned parallel to the hot wall, local turbulence near the hot wall is significantly enhanced, even as overall core flow turbulence diminishes.

The distribution of the Prandtl number and wall shear stress reveals the complex interplay between buoyancy-driven effects and secondary flow motions, highlighting distinct deviations from traditional incompressible flow behavior. For instance, case 4-ZG exhibits a marked deviation from the normalized secondary flow intensity peak observed in case 1-NoG, underscoring the pronounced impact of buoyancy-driven secondary flows. Moreover, the direction of gravity alters the traditional vortex structures and their intensities within the duct. Cases with gravity oriented in the y-direction show intensified secondary flows, while case 4-ZG is characterized by a dominant secondary vortex along with smaller vortices near the corners. These results emphasize the intricate relationship between gravity direction, buoyancy effects, and secondary flow motions in high-pressure transcritical square duct flows. Evaluating the implications of these findings on engineering applications, particularly in power generation and propulsion systems,

is vital for optimizing duct designs and operational strategies to enhance thermal efficiency and performance. This should contribute to the advancement of thermal management technologies in high-pressure transcritical environments.

Future research should focus on the detailed dynamics of secondary flow motions under varying high-pressure transcritical conditions. A deeper exploration of vorticity dynamics, particularly how secondary vortices form, interact, and evolve under different gravity directions, is essential for optimizing mixing and heat transfer processes. Analyzing the transient behaviors and stability of secondary flow motions can reveal how these flows respond to sudden changes in operating conditions.

ACKNOWLEDGMENTS

This work is funded by the European Union (ERC, SCRAMBLE, 101040379). Views and opinions expressed are however those of the authors only and do not necessarily reflect those of the European Union or the European Research Council. Neither the European Union nor the granting authority can be held responsible for them. The authors also acknowledge support from the SGR (2021-SGR-01045) program of the Generalitat de Catalunya (Spain).

References

[1] A. Abdellatif and L. Jofre. "Empirical heat transfer correlations of high-pressure transcritical fluids at low Reynolds numbers". In: *Int. J. Heat Mass Transf.* 231 (2024), p. 125837. DOI: 10.1016/j.ijheatmasstransfer.2024.125837.

[2] J. Bae, J. Y. Yoo, and D. M. McEligot. "Direct numerical simulation of heated CO 2 flows at supercritical pressure in a vertical annulus at $Re = 8900$". In: *Phys. Fluids* 20.5 (2008), p. 055108. DOI: 10.1063/1.2927488.

[3] G. Barea, N. Masclans, and L. Jofre. "Multiscale flow topologies in microconfined high-pressure transcritical fluid turbulence". In: *Phys. Rev. Fluids* 8 (5 May 2023), p. 054608. DOI: 10.1103/PhysRevFluids.8.054608. URL: https://link.aps.org/doi/10.1103/PhysRevFluids.8.054608.

[4] M. Bernades, F. Capuano, and L. Jofre. "Microconfined high-pressure transcritical fluids turbulence". In: *Phys. Fluids* 35 (2023), p. 015163. DOI: 10.1063/5.0135388.

[5] S. Gavrilakis. "Numerical simulation of low-Reynolds-number turbulent flow through a straight square duct". In: *J. Fluid Mech.* 244 (1992), pp. 101–129. DOI: 10.1017/S0022112092002982.

[6] J. Guo, X.I.A. Yang, and M. Ihme. "Structure of the thermal boundary layer in turbulent channel flows at transcritical conditions". In: *J. Fluid Mech.* 934 (2022), A45. DOI: 10.1017/jfm.2021.1157.

[7] L. Jofre, M. Bernades, and F. Capuano. "Dimensionality reduction of non-buoyant microconfined high-pressure transcritical fluid turbulence". In: *Int. J. Heat Fluid Flow* 102 (2023), p. 109169. DOI: 10.1016/j.ijheatfluidflow.2023.109169.

[8] L. Jofre, Z. R. del Rosario, and G. Iaccarino. "Data-driven dimensional analysis of heat transfer in irradiated particle-laden turbulent flow". In: *Int. J. Multiph. Fl.* 125 (2020), p. 103198. DOI: 10.1016/j.ijmultiphaseflow.2019.103198.

[9] F. Li et al. "Analysis of real-fluid thermodynamic effects on turbulent statistics in transcritical channel flows". In: *Phys. Rev. Fluids* 8.2 (2023), p. 024605. DOI: 10.1103/PhysRevFluids.8.024605.

[10] P. C. Ma, X. I. A. Yang, and M. Ihme. "Structure of wall-bounded flows at transcritical conditions". In: *Phys. Rev. Fluids* 3.3 (2018), p. 034609. DOI: PhysRevFluids.3.034609.

[11] N. Masclans et al. "Thermodynamics-informed neural network for recovering supercritical fluid thermophysical information from turbulent velocity data". In: *Int. J. Thermofluids* 20 (2023), p. 100448. DOI: 10.1016/j.ijft.2023.100448.

[12] D. Modesti, S. Pirozzoli, and F. Grasso. "Direct numerical simulation of developed compressible flow in square ducts". In: *Intl J. Heat Fluid Flow* 76 (2019), pp. 130–140. DOI: 10.1016/j.ijheatfluidflow.2019.02.002.

[13] C. Monteiro and L. Jofre. "Flow Regime Analysis of High-Pressure Transcritical Fluids in Microducts". In: *Int. J. Heat Mass Transfer* XX.X (2024), pp. XX–XX. DOI: XXXXXXX.

[14] H. Nemati et al. "The effect of thermal boundary conditions on forced convection heat transfer to fluids at supercritical pressure". In: *J. Fluid Mech.* 800 (2016), pp. 531–556. DOI: 10.1017/jfm.2016.411.

[15] B. E. Owolabi, Robert R. J. Poole, and D. J.C Dennis. "Experiments on low-Reynolds-number turbulent flow through a square duct". In: *J. Fluid Mech.* 798 (2016), pp. 398–410. DOI: 10.1017/jfm.2016.314.

[16] A. Patel et al. "Semi-local scaling and turbulence modulation in variable property turbulent channel flows". In: *Phys. Fluids* 27.9 (2015), p. 095101. DOI: 10.1063/1.4929813.

[17] J. W. R. Peeters et al. "Turbulence attenuation in simultaneously heated and cooled annular flows at supercritical pressure". In: *J. Fluid Mech.* 799 (2016), pp. 505–540. DOI: 10.1017/jfm.2016.383.

[18] A. Pinelli et al. "Reynolds number dependence of mean flow structure in square duct turbulence." In: *J. Fluid Mech.* 644 (2010), pp. 107–122. DOI: 10.1017/S0022112009992242.

[19] S. Pirozzoli et al. "Turbulence and secondary motions in square duct flow". In: *J. Fluid Mech.* 840 (2018), pp. 631–655. DOI: 10.1017/jfm.2018.66.

[20] A. Sekimoto et al. "Turbulence-and buoyancy-driven secondary flow in a horizontal square duct heated from below". In: *Phys. Fluids* 23.7 (2011), p. 075103. DOI: 10.1063/1.3593462.

[21] M. Uhlmann et al. "Marginally turbulent flow in a square duct". In: *J. Fluid Mech.* 588 (2007), pp. 153–162. DOI: 10.1017/S0022112007007604.

[22] T. Wan et al. "Mean velocity and temperature scaling for near-wall turbulence with heat transfer at supercritical pressure". In: *Phys. Fluids* 32.5 (2020), p. 055103. DOI: 10.1063/5.0002855.

[23] J. Y. Yoo. "The turbulent flows of supercritical fluids with heat transfer". In: *Annu. Rev. Fluid Mech.* 45 (2013), pp. 495–525. DOI: 10.1146/annurev-fluid-120710-101234.

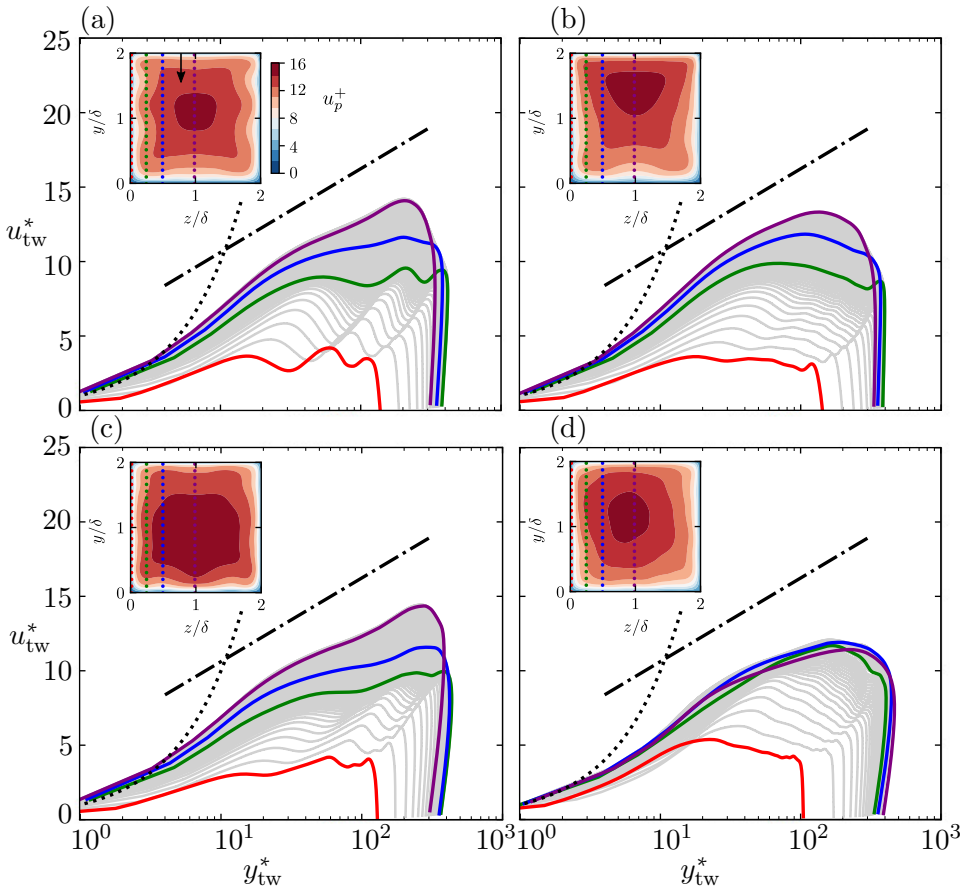

Figure 3: Mean semi-local streamwise velocity profiles u^* from the top wall (a-d) and temperature distribution normalized by bulk temperature T/T_b (e-h). Panels (a,e) correspond to NoG (no gravity), (b,f) to Case 3-YG (positive y-direction gravity), (c,g) to Case 2-mYG (negative y-direction gravity), and (d,h) to Case 4-ZG (gravity parallel to the z-direction). The dotted line represents the law of the viscous layer, $u^* = y^*$, while the dotted-dashed line depicts the law of the logarithmic layer, $u^* = (1/k)\ln y^* + B$, with $k = 0.41$ and $B = 5$.

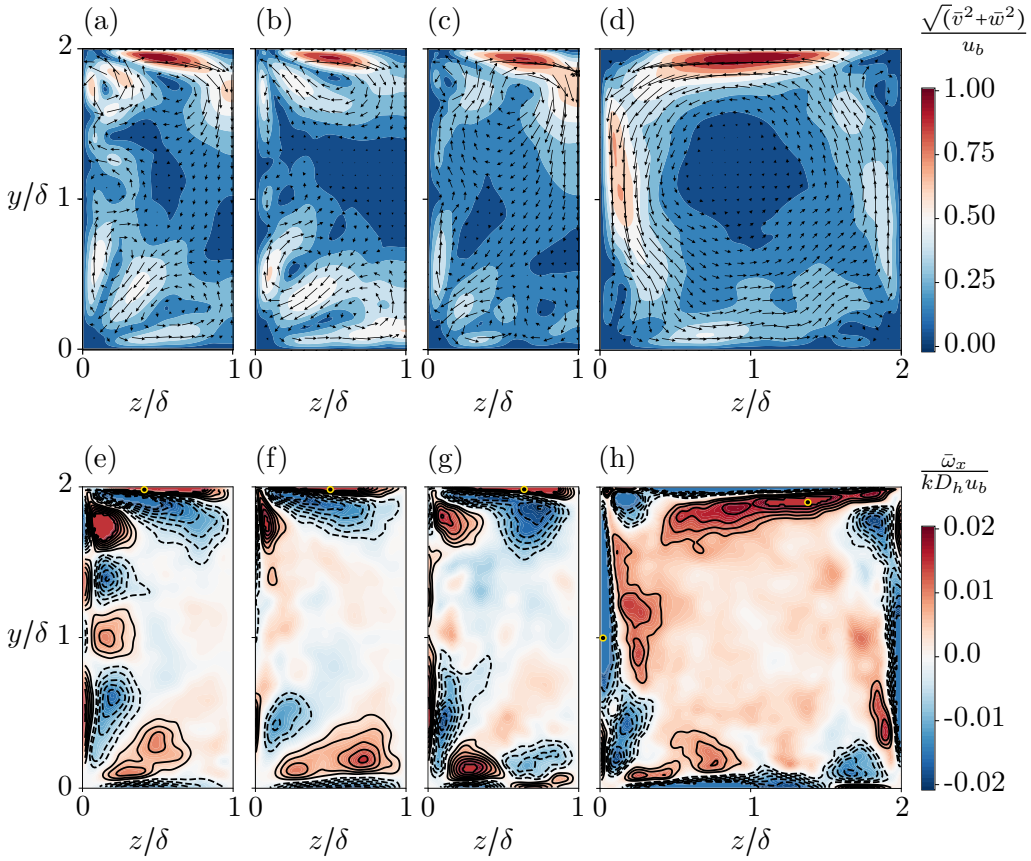

Figure 4: Distribution of mean cross-flow velocity intensity normalized by the maximum value of each case, as listed in Table 1 (a-d), and outer-scaled mean streamwise vorticity $\omega_x = \frac{\partial v}{\partial z} - \frac{\partial w}{\partial y}$ for cases D192Nog (a,e), D192Y (b,f), D192my (d,g), and D192Z (d,h).